

# Dissecting the Perseus-Pisces supercluster observed with CFHT-MegaCam

## Exploring late-type galaxy shape alignments within the local cosmic web

M. Mondelin<sup>1</sup>, S. Codis<sup>1</sup>, J.-C. Cuillandre<sup>1</sup>, R. Paviot<sup>1</sup>, and T. de Boer<sup>2</sup>

<sup>1</sup> Université Paris-Saclay, Université Paris Cité, CEA, CNRS, AIM, 91191 Gif-sur-Yvette, France  
e-mail: maelie.mondelin@cea.fr

<sup>2</sup> Institute for Astronomy, University of Hawaii, 2680 Woodlawn Drive, Honolulu HI 96822, USA

### ABSTRACT

Intrinsic alignments of galaxy shapes constitute a critical systematic for weak gravitational lensing and probe how galaxies acquire their orientations within the cosmic web. So far, studies have focused mostly on statistical samples of galaxies. In this work, we take the opposite approach and measure this signal in one local superstructure but with exquisite resolution up to the most external regions where secondary infall should be predominant. More specifically, we measure intrinsic alignment signals in the Perseus–Pisces Supercluster as a function of galaxy morphology and their radial variations into the low surface brightness regime.

We use deep CFHT *r*-band imaging covering 367 deg<sup>2</sup> (mostly from the UNIONS survey) and reaching 28 mag arcsec<sup>-2</sup> to measure correlation functions at three isophotal radii ( $R_{23}$ ,  $R_{25}$ ,  $R_{27}$ ) for 2004 galaxies with  $\log M_*/M_\odot > 8.6$ , stratifying by morphological type and stellar mass in comoving coordinates.

We detect positive intrinsic alignment signals for both early- and late-type galaxies, extending to  $\sim 1$  Mpc/*h* in comoving space, including a clear and robust signal for spiral galaxies. Shape-shape correlations ( $\xi_+$ ) are substantially stronger than position-shape correlations ( $\xi_{g+}$ ), with comoving measurements increasing the fraction of strongly correlated galaxies detected. Correlation profiles show minimal radial dependence across the three isophotes despite 10–20% of galaxies showing ellipticity variations. We report a robust detection of morphology-dependent intrinsic alignment components: late-type galaxies strongly dominate the shape-shape signal (86% of strongly correlated galaxies despite representing 69% of the sample), residing preferentially in filamentary regions and exhibiting systematically higher ellipticities indicating edge-on configurations. Early-type galaxies show no significant over-representation in position-shape correlations, but concentrate near cluster/group centers where environmental enrichment becomes apparent.

The environmental segregation suggests early-types align via tidal stretching in dense cluster environments while late-types align via tidal torquing in filaments. These local-Universe measurements contribute to interpreting alignment systematics for upcoming surveys like *Euclid*, DESI, and LSST, and highlight notably the key contributions of blue spiral late-type galaxies in intrinsic alignment signals at least in the low-redshift Universe, hence the need to model them carefully for cosmic shear analyses.

**Key words.** Galaxies: clusters: individual: Perseus, Galaxies: interactions, Galaxies: evolution, Galaxies: fundamental parameters

## 1. Introduction

In the  $\Lambda$ CDM cosmological framework, small matter fluctuations in the cosmic web drive the formation and evolution of galaxies (Klypin & Shandarin 1983; Bond et al. 1996). This large-scale structure, composed of filaments, sheets, nodes, and voids, generates coherent tidal fields that exert torques on protogalactic gas clouds during collapse. This imprints preferred orientations on the angular momentum of forming galaxies (Peebles 1969; Doroshkevich 1970). Theoretical models and simulations predict that dark matter haloes align their spin axes and principal axes with the eigenvectors of the local tidal tensor, with spin directions typically perpendicular to the direction of strongest compression (Aragón-Calvo et al. 2007; Hahn et al. 2010; Codis et al. 2012).

The intrinsic alignment of galaxy shapes and spins constitutes both a challenge and an opportunity for observational cosmology. As weak gravitational lensing has emerged as a primary probe of dark matter and dark energy through cosmic shear measurements (Kilbinger 2015; Mandelbaum 2018), the need to dis-

entangle intrinsic shape correlations from lensing-induced correlations has become critical. Intrinsic alignments can mimic or dilute the weak lensing signal, potentially biasing cosmological parameter estimates (Hirata et al. 2004; Joachimi et al. 2015; Troxel & Ishak 2015). In particular, tidal stretching of early-type galaxies by the surrounding density field has been identified as a dominant alignment mechanism (Catelan & Porciani 2001; Hirata et al. 2004; Chisari 2025). We refer the readers to Lamman et al. (2024) for a comprehensive overview of alignment processes and their observational signatures. This systematic contamination has motivated extensive observational efforts to characterize intrinsic alignment amplitudes as a function of galaxy properties, redshift, and environment (Mandelbaum et al. 2006; Joachimi et al. 2011; Singh et al. 2015).

Large photometric surveys have provided the statistical power necessary to detect intrinsic alignments. Early measurements from the Sloan Digital Sky Survey (SDSS; York et al. (2000); Hirata et al. (2004); Mandelbaum et al. (2006)) and the Canada–France–Hawaii Telescope Legacy Survey (CFHTLS; Hildebrandt et al. (2012)) revealed

significant position-shape correlations for luminous red galaxies, confirming that massive early-type systems exhibit strong alignments consistent with tidal stretching by the surrounding density field. Stage-III surveys, including Dark Energy Survey and Kilo-Degree Survey Collaboration et al. (2023) and More et al. (2023), have extended these measurements to fainter magnitudes and higher redshifts, enabling studies of alignment evolution and morphological dependencies. The recent UNIONS–BOSS/eBOSS cross-correlation has pushed these constraints further, yielding robust detections across  $3500 \text{ deg}^2$  and confirming strong luminosity scaling of alignment amplitudes (Hervas Peters et al. 2025). Complementary measurements from the PAU Survey have provided some of the tightest constraints to date on blue galaxy alignments, finding amplitudes consistent with zero for star-forming systems while detecting increasing signals with stellar mass and luminosity for red galaxies (Navarro-Gironés et al. 2026).

A parallel line of investigation has focused on the alignment of galaxy spins with the cosmic web filamentary structure. Hydrodynamical simulations predict a mass-dependent "spin flip": low-mass galaxies tend to have angular momentum vectors parallel to nearby filaments, consistent with tidal torquing during accretion along filaments, while massive galaxies exhibit perpendicular orientations, reflecting virialization and merger activity near filament nodes (Codis et al. 2012; Dubois et al. 2014; Welker et al. 2014; Codis et al. 2015a; Laigle et al. 2015). Observational predictions for alignment signals as a function of environment and morphology further support this picture (Regaldo-Saint Blancard et al. 2021). This transition has been confirmed observationally (SAMI Galaxy Survey; Welker et al. (2020) and MaNGA (Kraljic et al. 2021)), which provide evidence for mass-dependent and environment-dependent spin orientation patterns, as also suggested by theoretical arguments (Codis et al. 2015b). Recent observations have even detected signatures of filament rotation itself on scales of  $\sim 15 \text{ Mpc}$ , suggesting that angular momentum cascades from the largest scales down to individual galaxies (Tudorache et al. 2025).

However, the connection between dark matter predictions and observed galaxy alignments is mediated by complex baryonic physics. Gas cooling, star formation, stellar and AGN feedback, and mergers can all suppress, enhance, or reorient alignment signals relative to pure dark matter expectations (Chisari et al. 2015; Codis et al. 2018). Radiative cooling drives dissipative collapse that decouples stellar angular momentum from the underlying dark matter halo, while feedback injects energy that disrupts coherent inflows and randomizes orientations, particularly in low-mass systems (Dubois et al. 2014; Zjupa et al. 2020). Recent reviews synthesizing theoretical, simulation, and observational perspectives highlight that intrinsic alignments remain one of the most uncertain components of weak lensing systematics budgets (Joachimi et al. 2015; Kiessling et al. 2015; Blazek et al. 2019; Lamman et al. 2024). Understanding how baryonic processes modulate alignment signals as a function of mass, morphology, and environment is thus essential both for mitigating weak lensing contamination and for constraining galaxy formation physics.

Looking ahead, the next generation of large-sky imaging surveys promises transformative advances. The Dark Energy Spectroscopic Instrument (DESI) is simultaneously obtaining spectra for tens of millions of galaxies, enabling environmental studies with unprecedented three-dimensional completeness. Meanwhile, the *Euclid* space mission will provide complementary wide-field imaging and spectroscopy free from atmospheric distortions (Laureijs et al. 2011; Euclid Collaboration et al. 2025c).

The Vera C. Rubin Observatory's Legacy Survey of Space and Time (LSST, Ivezić et al. (2019)) will observe billions of galaxies over  $18,000 \text{ deg}^2$  with exquisite image quality. (DESI Collaboration et al. 2016). Early science results from *Euclid* Quick 1 data (Euclid Collaboration: Mellier et al. 2025; Euclid Collaboration et al. 2025a) already demonstrate the power of these new datasets for studying alignments with the cosmic web (Euclid Collaboration et al. 2025b). These surveys will push intrinsic alignment measurements to higher redshifts, lower masses, and finer environmental resolution than previously achievable, but their interpretation will rely critically on calibrations from well-characterized local samples where galaxy properties, morphologies, and environments can be measured with high fidelity.

In this context, the local Universe offers unique advantages for calibration studies: spatially resolved galaxies enabling detailed morphological classification, accurate three-dimensional distances for robust structure identification, and nearby superclusters providing high-contrast environments where tidal fields are strongest. In our companion study (Paper I, Mondelin et al. 2025), we presented a comprehensive reconstruction of the Perseus–Pisces Supercluster at  $z < 0.03$ , identifying filaments, clusters, and groups using spectroscopic redshifts. This structure, containing over 3000 galaxies from void edges to cluster cores, provides us with a laboratory for studying how the cosmic web shapes galaxy properties. In this paper II, we will exploit low surface brightness features to probe outer stellar regions. More specifically, using LSB-optimized CFHT MegaCam imaging reaching  $28.3 \text{ mag arcsec}^{-2}$  (Elixir-LSB pipeline; Ferrarese et al. (2012)), we will measure galaxy shapes at multiple isophotal radii. Since outer disks are less gravitationally bound, they may be more susceptible to external tidal influences (Peng et al. 2010), allowing tests of whether alignment signatures vary with radius. For this reason, we will measure intrinsic alignment signals using two-point correlation functions, stratifying by morphology, stellar mass, and isophotal radius. The combination of precise morphologies, multi-radius measurements, accurate 3D structure, and high-contrast environment will allow us to test for alignment mechanisms in a well-characterized local sample.

The paper is organized as follows. First, Section 2 describes the sample and methodology. Then, Section 3 presents the intrinsic alignment measurements. Finally, Section 4 interprets the results in the context of theory and observations, and Section 5 concludes. Supplementary material in the appendices presents the validation of our correlation measurements (Appendix A), additional morphology–environment diagnostics (Appendix B), and morphology-dependent correlation decompositions (Appendix C).

## 2. Data and Methods

### 2.1. Galaxy sample and shape measurements

We analyse the galaxy sample from Paper I: two regions, A and B, within the Perseus–Pisces Supercluster (PPSC) observed with CFHT/MegaCam in the  $r$ -band, with extensive spectroscopic redshift coverage. Figure 1 shows the spatial distribution in equatorial coordinates, with background shading indicating local number density. Filament spines extracted by DisPerSE (Sousbie et al. 2011) in Paper I are projected onto the RA–Dec plane and overlaid; galaxy shapes are represented by oriented ellipses, offering a first visual impression of potential alignments within the filamentary structure.

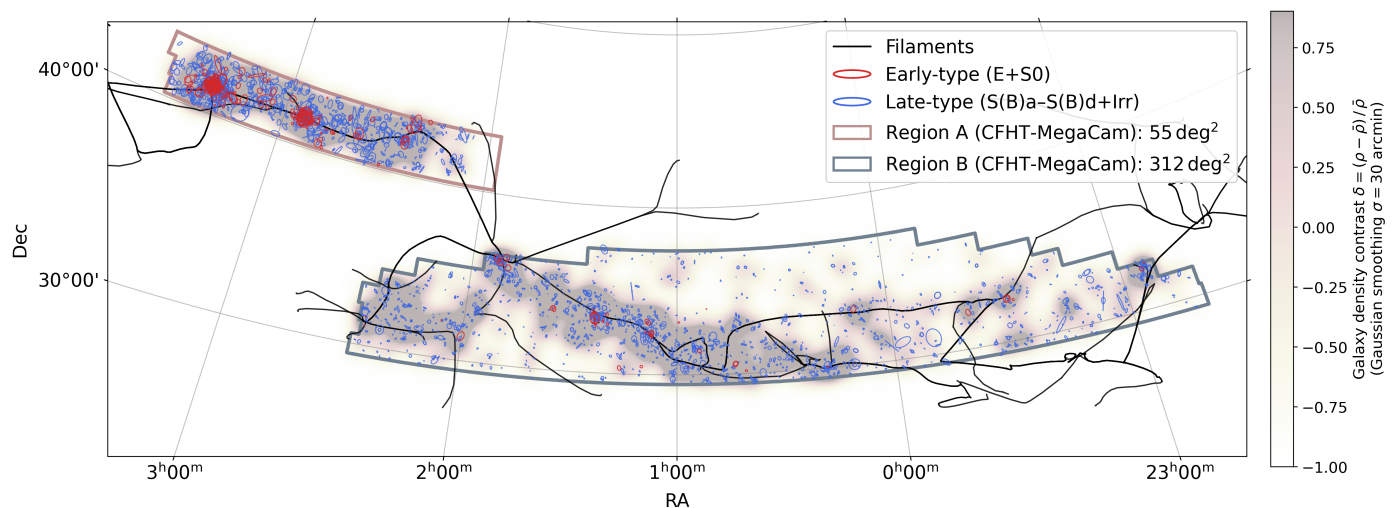


Fig. 1: Spatial distribution and cosmic-web structure of the PPSC. Galaxy positions are shown in equatorial coordinates; background colour encodes the local number-density contrast  $\delta = (\rho - \bar{\rho})/\bar{\rho}$ , where  $\bar{\rho}$  is the mean number of galaxies per bin, ranging from  $\delta = -1$  (empty regions) to several units in the densest areas. The density field is computed on a 5-arcmin grid smoothed with a Gaussian kernel of  $\sigma = 30$  arcmin. Black curves trace filament spines from the projected 3D DisPerSE reconstruction (Paper I). Galaxy shapes, measured at  $R_{25}$ , are shown as oriented blue ellipses for late-type galaxies and red ellipses for early-type galaxies. Regions A and B are visible as distinct overdensities connected by lower-density bridges. Note that region B is the UNIONS coverage of the south galactic cap (Gwyn et al. 2025).

From the deep imaging, Paper I extracted surface-brightness profiles using `AUTO PROF` (Stone et al. 2021) and `ASTROPHOT` (Stone et al. 2023), fitting elliptical isophotes at multiple radii. For our intrinsic-alignment analysis we focus on three isophotal levels:  $R_{23}$ ,  $R_{25}$ , and  $R_{27}$ , corresponding to surface-brightness thresholds of 23, 25, and 27 mag arcsec $^{-2}$  in the  $r$ -band. These sample progressively fainter stellar regions from the bright inner body ( $R_{23}$ ) through the intermediate zone ( $R_{25}$ ) to the extended outer envelope ( $R_{27}$ ).

At each isophote the fit provides a semi-major axis  $R_i$ , semi-minor axis  $b$ , and position angle  $\theta_{PA}$  (Bartelmann & Schneider 2001). We compute the ellipticity modulus  $e = (1 - q)/(1 + q)$  with  $q = b/R_i$ , and decompose it into Cartesian components

$$e_1 = e \cos(2\theta_{PA}), \quad e_2 = e \sin(2\theta_{PA}). \quad (1)$$

These ellipticity vectors ( $e_1, e_2$ ) encode both the degree of flattening and the orientation of each galaxy, and are the fundamental observables for all correlation measurements that follow.

We adopt the morphological classifications from Paper I, which combined visual inspection with Sérsic-index fitting, and exclude the  $\sim 10\%$  of galaxies showing signs of strong tidal interactions; these systems may exhibit anomalous alignments driven by local galaxy–galaxy torques rather than coherent large-scale tidal fields, potentially contaminating the signal of interest. The remaining galaxies are divided into early types (ET: ellipticals E and S0) and late types (LT: spirals S(B)a–S(B)d and irregulars Irr). Starting from 2843 galaxies, we apply a stellar-mass cut of  $\log M_*/M_\odot > 8.5$  and require measurements at all three isophotal radii, yielding a final sample of 2004 galaxies: 619 ET (31%) and 1385 LT (69%). The projected spatial distribution of the different morphological classes is shown in Appendix B, which provides a visual overview of the morphology–environment segregation across the PPSC. The mass threshold ensures completeness above 50% (Paper I). Figure 2 shows representative examples of each morphological type with the three isophotes overlaid.

## 2.2. Correlation functions: quantifying shape coherence

Intrinsic alignment manifests as statistical correlations between galaxy orientations. We quantify it with two complementary two-point estimators. The *shape–shape* correlation  $\xi_+$  tests whether galaxies at a given separation tend to point in similar directions. The *position–shape* correlation  $\xi_{g+}$  tests whether galaxies surrounding a reference object are preferentially oriented radially or tangentially with respect to that reference.

Both estimators require projecting each galaxy’s ellipticity onto a frame aligned with the pair separation vector. For galaxies  $i$  and  $j$  separated by a vector with position angle  $\phi$ , the tangential ( $e_+$ ) and cross ( $e_\times$ ) components are (Bartelmann & Schneider 2001; Troxel & Ishak 2015)

$$e_+ = \text{Re}[\varepsilon e^{-2i\phi}], \quad e_\times = \text{Im}[\varepsilon e^{-2i\phi}], \quad (2)$$

where  $\varepsilon = e_1 + i e_2$ . The shape–shape correlation is then

$$\xi_+(r) = \langle e_{+,i} e_{+,j} \rangle + \langle e_{\times,i} e_{\times,j} \rangle, \quad (3)$$

averaged over all galaxy pairs at separation  $r$ . Equation 3 probes intrinsic–intrinsic (II) alignment, where both galaxies have been shaped by a common tidal field (Hirata et al. 2004; Codis et al. 2015a).

For the position–shape correlation we follow the `TREECORR` convention (Jarvis 2015): a positive value of

$$\xi_{g+}(r) = \langle e_{g+,j} \rangle_i, \quad (4)$$

where  $e_{g+,j} = e_{1,j} \cos 2\phi + e_{2,j} \sin 2\phi$ , signals preferential *radial* elongation of surrounding galaxies toward the reference, while a negative value indicates tangential elongation.  $\xi_{g+}$  is sensitive to tidal-shear effects in which the surrounding density field modulates the orientations of neighboring galaxies (Blazek et al. 2011).

We compute both correlations using explicit pair counting (rather than relying solely on `TREECORR`), which allows us to

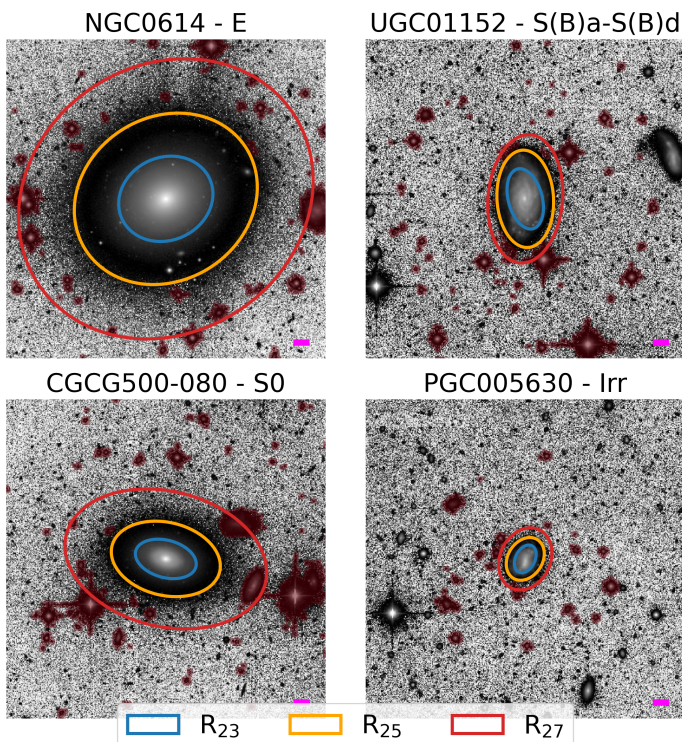


Fig. 2: Isophotal shape measurements across morphological types: elliptical (top left), S0 (bottom left), spiral (top right), and irregular (bottom right). Overlaid ellipses mark the three isophotal radii:  $R_{23}$  (blue),  $R_{25}$  (gold), and  $R_{27}$  (red), illustrating the radial evolution of galaxy shape from inner to outer regions. Red-shaded areas are pixels masked during profile extraction. Magenta scale bar: 10 arcsec.

record the individual contributors to each separation bin. We verified our implementation against `TREECORR` and found excellent agreement (Appendix A). Separations are binned logarithmically into six bins spanning  $0.01\text{--}40 h^{-1}$  Mpc in comoving space. The lower angular limit is anchored to the typical projected galaxy size ( $\sim 10$  kpc  $\approx 0.5$  arcmin at  $\langle z_{\text{PPSC}} \rangle \sim 0.017$ ).

Throughout the paper we present results as a function of the comoving separation  $r$ , computed from three-dimensional pair distances using the spectroscopic redshifts of Paper I. This approach naturally accounts for the radial distribution of galaxies and ensures that pairs at different redshifts are weighted according to their true physical separation.

Uncertainties are estimated via bootstrap resampling with  $N_{\text{BS}} = 500$  realisations. In each realisation we draw, with replacement, a sample of the same size as the original catalogue from the pool of individual galaxies, rebuild the pair catalogue, and recompute the correlation function. The bootstrap variance is

$$\sigma_{\xi}^2 = \frac{1}{N_{\text{BS}} - 1} \sum_{k=1}^{N_{\text{BS}}} (\xi^{(k)} - \bar{\xi})^2, \quad (5)$$

where  $\bar{\xi}$  is the mean over all realisations. We consider a signal significant when it exceeds  $1\sigma$ .

### 2.3. Multi-radius and morphology stratification

We compute correlation functions independently at  $R_{23}$ ,  $R_{25}$ , and  $R_{27}$ , allowing us to test whether alignment signals vary with

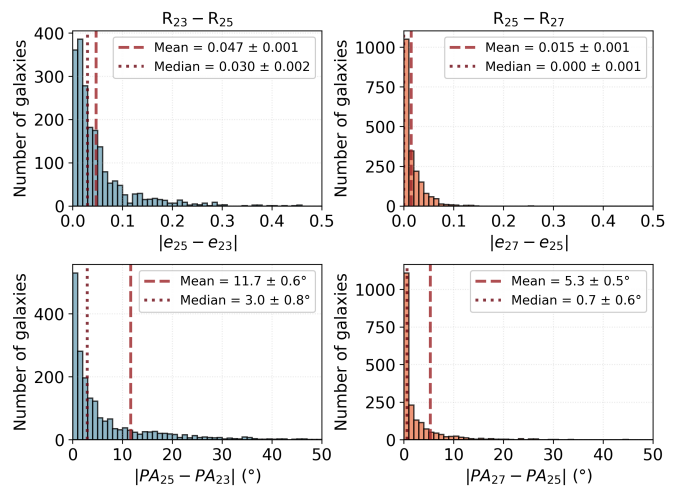


Fig. 3: Variation of galaxy shapes between consecutive isophotal radii. Top row: ellipticity differences. Bottom row: position-angle differences. Left column:  $R_{23}$  to  $R_{25}$ . Right column:  $R_{25}$  to  $R_{27}$ . Dashed and dotted lines mark mean and median values, respectively.

radius. Inner stellar regions may be shaped primarily by baryonic processes and strong gravitational binding, whereas outer envelopes are less bound and may more closely trace the dark-matter halo, potentially coupling more strongly to the large-scale tidal field (Zjupa & Springel 2017). At each radius we recalculate the ellipticity components (Eq. 1), rotate to the  $(+, \times)$  frame defined by the projected separation vector (Eq. 2), and compute  $\xi_+$  and  $\xi_{g+}$  independently.

Figure 3 shows how ellipticity and position angle vary between consecutive isophotes. Between  $R_{23}$  and  $R_{25}$  the median changes are  $|\Delta e| \approx 0.030$  and  $|\Delta \text{PA}| \approx 3.0^\circ$ , with 31% of galaxies exceeding  $|\Delta e| > 0.05$  and 37% exceeding  $|\Delta \text{PA}| > 5^\circ$ . From  $R_{25}$  to  $R_{27}$  these variations decrease to median values of 0.010 and  $1.5^\circ$ , with only 8% and 17% exceeding the respective thresholds.  $\sim 90\%$  galaxies therefore maintain coherent shapes across radii. Both distributions nonetheless show extended tails, particularly in position angle (mean  $12.0^\circ$  from  $R_{23}$  to  $R_{25}$ , well above the median), driven by outliers with isophotal twists exceeding  $20^\circ$ ; visual inspection confirms these are predominantly late-type spirals whose central bars or asymmetric arms create radial shape variations.

### 2.4. Direct alignment with the cosmic web

For each galaxy we define the alignment angle  $\theta_{\text{cl}/\text{fil}} \in [0^\circ, 90^\circ]$  as the angle, projected on the plane of the sky, between the galaxy major axis and a reference cosmic-web direction. Figure 4 illustrates the geometric setup and the key environmental parameters used throughout this analysis.

The major-axis unit vector in the (East, North) frame is

$$\hat{a} = (\sin \text{PA}, \cos \text{PA}), \quad (6)$$

where PA is the position angle measured from North toward East.

We compute two alignment angles for each galaxy, corresponding to two different cosmic-web directions. For  $\theta_{\text{fil}}$ , the reference direction is the local tangent to the nearest DisPerSE filament spine: we project each skeleton segment onto the sky, identify the node closest to the galaxy, and compute the tangent

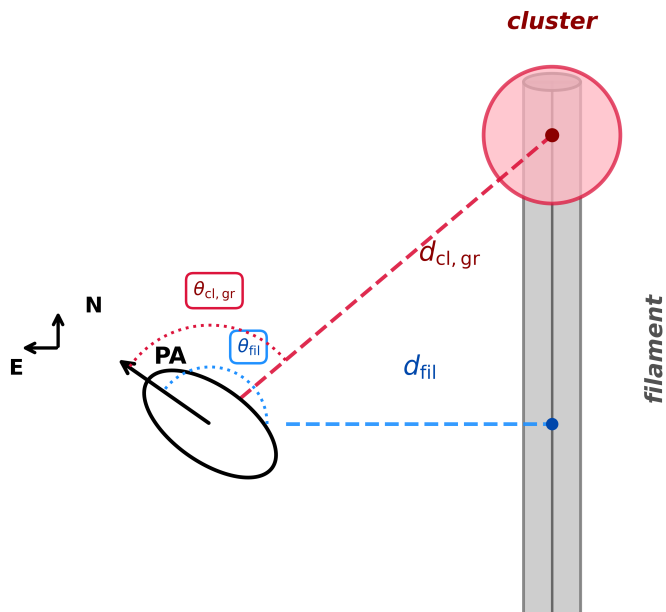


Fig. 4: Schematic illustration of alignment measurements and environmental parameters. The filament is shown as a grey cylinder. A galaxy (black ellipse) is characterized by its position angle PA, its distance to the nearest filament spine ( $d_{\text{fil}}$ , blue dashed line), and its distance to the nearest cluster or group center ( $d_{\text{cl,gr}}$ , red dashed line). The two angles  $\theta_{\text{fil}}$  and  $\theta_{\text{cl,gr}}$  are also represented.

using the two adjacent nodes, applying the standard  $\cos$  Dec correction for the convergence of meridians. For  $\theta_{\text{cl}}$ , the reference direction is the projected line of sight from the galaxy to the centre of its host cluster or group, defined by the position of the central galaxy (Paper I). Because  $\hat{a}$  and  $-\hat{a}$  are equivalent, we use the absolute dot product:

$$a\theta_{\text{cl/fil}} = \arccos(|\hat{a} \cdot \hat{r}|), \quad (7)$$

where  $\hat{r}$  is either the filament tangent or the cluster-centric direction. A value  $\theta_{\text{cl/fil}} < 45^\circ$  indicates that the major axis tends to lie along the structure;  $\theta_{\text{cl/fil}} > 45^\circ$  indicates alignment perpendicular to it. The isotropic reference is  $\langle \theta_{\text{cl/fil}} \rangle = 45^\circ$  (dashed line in Fig. 9).

Measurements are performed at each of the three isophotal radii ( $R_{23}$ ,  $R_{25}$ ,  $R_{27}$ ). We present results for  $R_{25}$  throughout the main text; results for  $R_{23}$  and  $R_{27}$  are consistent. Following the environmental classification of Paper I, each galaxy is assigned to one of four environments based on its distance to the nearest cluster or group centre ( $d_{\text{gr,cl}}$ ) and to the nearest filament spine ( $d_{\text{fil}}$ ). By comparing the environmental distributions of strongly correlated galaxies with those of the full sample, we test whether enhanced alignment is associated with specific large-scale structures.

### 3. Results

We present measurements of intrinsic alignment signals in the PPSC. We first analyse correlation functions computed for the full galaxy sample, then investigate which galaxies contribute most strongly to the detected signals, and finally connect alignment patterns to the large-scale structure environment characterised in Paper I.

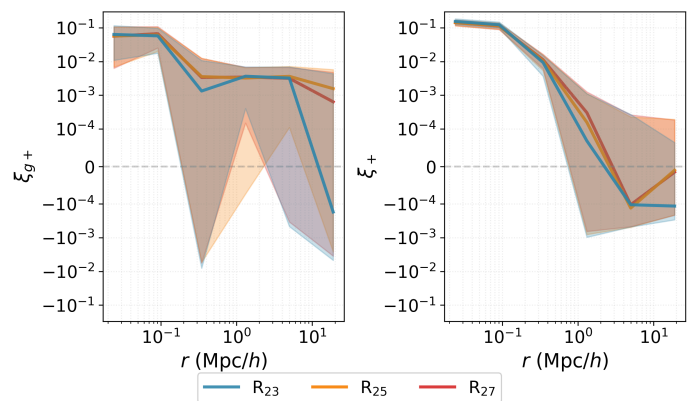


Fig. 5: Two-point correlation functions for the full galaxy sample as a function of comoving separation  $r$ . Left panel: position–shape correlation  $\xi_{g+}$ . Right panel: shape–shape correlation  $\xi_+$ . Three isophotal radii are shown:  $R_{23}$  (blue),  $R_{25}$  (orange),  $R_{27}$  (red). Shaded regions indicate bootstrap uncertainties.

#### 3.1. Detection of intrinsic alignment signals

Figure 5 shows the correlation functions measured for the full galaxy sample as a function of comoving separation  $r$ . Both  $\xi_{g+}$  and  $\xi_+$  exhibit a clear positive signal at small separations. The position–shape correlation  $\xi_{g+}$  shows a non-zero large-scale amplitude of order  $\sim 4 \times 10^{-3}$ , with a significant enhancement at  $r \sim 0.09 h^{-1} \text{ Mpc}$  ( $S/N \sim 3$ ). The shape–shape correlation  $\xi_+$  remains consistent with zero on large scales while showing a strong detection at  $r \lesssim 0.1 h^{-1} \text{ Mpc}$  ( $S/N \sim 10$ ).

The signal at  $r \lesssim 0.1 h^{-1} \text{ Mpc}$  probes the one-halo regime, where galaxy pairs reside within the same dark matter halo. At these scales, alignments are driven by the local tidal field internal to the halo, naturally producing the strong signal observed. This scale matches the typical size of galaxy groups and clusters in the two PPSC regions (Paper I), supporting the interpretation that the dominant contribution arises from galaxies sharing the same gravitational potential.

At larger separations ( $r \gtrsim 1 h^{-1} \text{ Mpc}$ ),  $\xi_{g+}$  settles toward a roughly constant amplitude ( $\sim 4 \times 10^{-3}$ ), marking the transition to the two-halo regime in which galaxy pairs belong to distinct halos correlated through the large-scale tidal field, for example galaxies in neighbouring groups connected by filaments. This amplitude is consistent with results from large spectroscopic surveys reporting values of  $\sim 10^{-3} - 10^{-2}$  at  $r \sim 5 - 100 h^{-1} \text{ Mpc}$  for the SDSS LOWZ sample (Singh et al. 2024). The three isophotal radii yield broadly similar profiles although we observe a systematic trend for the large-scale amplitude to (slightly) increase with increasing  $R_{\text{iso}}$ , indicating that outer isophotes are indeed more sensitive to large-scale tidal distortions.

Decomposing these correlation functions by morphological type (see also Appendix C for more details) reveals that the detected signals seem to be dominated by the late-type population in first approximation. This morphological dichotomy motivates the detailed analysis of strongly correlated galaxies presented in Sect. 3.2.

#### 3.2. Strongly aligned galaxies

##### 3.2.1. Identifying strongly correlated galaxies

Detecting an average positive correlation does not reveal whether all galaxies are weakly aligned or whether a minor-

ity drives the signal. To distinguish these scenarios, we identify galaxies contributing disproportionately to the measured correlations.

For each separation bin where  $\xi$  is significantly positive (first three bins in comoving space), we compute for each galaxy  $i$  its cumulative contribution

$$C_i = \sum_{j \in \text{bin}} (e_{i,i} e_{i,j} + e_{x,i} e_{x,j}). \quad (8)$$

Galaxies with  $C_i > \langle C \rangle + \sigma_C$  are flagged as ‘‘strongly correlated’’ (SCG hereafter). These are systems whose orientations are unusually coherent with their neighbours. The selection is performed independently for each correlation function ( $\xi_+$  and  $\xi_{g+}$ , in comoving coordinates) and isophotal radius ( $R_{23}$ ,  $R_{25}$ ,  $R_{27}$ ).

### 3.2.2. Global properties of strongly correlated galaxies

Table 1 quantifies the SCG populations at  $R_{25}$ . For  $\xi_{g+}(r)$ , SCGs represent 19.4% of the whole population, split into 6.0% early-type and 13.4% late-type.

Table 1: Fractions of strongly correlated galaxies (SCG) at  $R_{25}$ . The full sample contains 2017 galaxies: 30.7% early-type (ET) and 69.3% late-type (LT).

Function	Total (%)	ET (%)	LT (%)
$\xi_{g+}(r)$	$19.4 \pm 0.9$	$6.0 \pm 0.5$	$13.4 \pm 0.8$
$\xi_+(r)$	$12.0 \pm 0.7$	$1.7 \pm 0.3$	$10.3 \pm 0.7$

For shape–shape alignments  $\xi_+(r)$ , late-types clearly dominate, representing  $\sim 86\%$  of SCGs (10.3%/12.0%), a strong enrichment relative to their baseline fraction of 69.3%. For position–shape alignments  $\xi_{g+}(r)$ , the morphological fractions among SCGs (31% ET, 69% LT) mirror the baseline composition of the sample, indicating that morphology alone does not predict selection into the  $\xi_{g+}$  SCG population.

This contrast between the two estimators likely reflects a competition between ellipticity and environment. For  $\xi_{g+}$ , the signal scales as  $e \times \delta$ : the density bias toward dense environments favours early-types, while the ellipticity factor favours late-types, and the two effects approximately cancel, leaving the morphological mix unchanged. For  $\xi_+$ , the signal scales as  $e^2$ , strongly weighting the more elongated late-type population regardless of environment.

Regarding the overlap between selections, about 39% of SCGs appear in both  $\xi_{g+}(r)$  and  $\xi_+(r)$ , while 46% appear only in  $\xi_{g+}(r)$  and 15% only in  $\xi_+(r)$ . This partial overlap is consistent with the interpretation that position–shape correlations are more sensitive to galaxies residing in dense environments where tidal fields are strongest, while shape–shape correlations preferentially select highly elongated galaxies whose shapes are coherent over larger volumes.

In this picture,  $\xi_{g+}$  is likely dominated by central–satellite pairs: the position of the central galaxy traces the local overdensity, while its shape is radially stretched by the halo potential, producing a strong density–shape signal on the one-halo scale. This is consistent with findings in the Horizon-AGN simulation, where spheroidal galaxies radially align toward overdensities and toward each other, and where satellites contribute significantly to the alignment signal through their preferential orientation around central galaxies (Chisari et al. 2015, 2017). By contrast,  $\xi_+$  mixes pairs at all halo-centric positions and is dominated by the more numerous satellite–satellite population; its signal is

therefore more sensitive to the global elongation of the galaxy population than to the local density environment. The preferential distribution of satellites within the galactic plane of massive red centrals (Welker et al. 2018) further reinforces the connection between the one-halo alignment signal and the large-scale tidal field that shapes both the central and its satellite system.

Table 2 presents mean stellar masses of SCGs at  $R_{25}$ . Strongly correlated galaxies show at most modest mass enhancements of 0.03–0.06 dex relative to the full sample, consistent within the measurement uncertainties for both morphological types and both correlation functions. Stellar mass therefore does not appear to be a primary driver of alignment strength in our sample; the morphological dichotomy described above is more naturally attributed to structural (ellipticity) and environmental effects.

Table 2: Mean stellar masses of SCGs at  $R_{25}$ .

Sample	$\langle \log M_*/M_\odot \rangle$	
	Early-type	Late-type
All galaxies	$10.39 \pm 0.02$	$9.74 \pm 0.02$
$\xi_{g+}(r)$	$10.43 \pm 0.04$	$9.79 \pm 0.03$
$\xi_+(r)$	$10.43 \pm 0.06$	$9.78 \pm 0.04$

### 3.2.3. Morphological properties of strongly correlated galaxies

Figure 6 shows the distribution of SCGs in the ellipticity–position angle plane at  $R_{25}$ .

For late-types, the most prominent feature is a systematic offset toward higher ellipticities. The full sample has mean  $\langle e \rangle \approx 0.33$ , while SCGs reach  $\langle e \rangle_{\text{SCG}} \approx 0.41$ – $0.57$  depending on the selection, with  $\xi_+$ -selected galaxies showing the highest values. Table 3 quantifies this enhancement: the ratio  $\langle e \rangle_{\text{SCG}}/\langle e \rangle_{\text{all}}$  is 1.25 for  $\xi_{g+}$  and 1.73 for  $\xi_+$  at  $R_{25}$ .

The ratio  $\langle e|SCG \rangle/\langle e \rangle$  allows us to distinguish between two scenarios: purely statistical enrichment due to the  $e$  or  $e^2$  weighting of the estimators, versus genuine physical alignment. If the enrichment were purely statistical, we would expect ratios of  $1 + \sigma/\mu \approx 1.24$  for linear ( $e$ ) weighting and  $1 + 2\sigma/\mu \approx 1.48$  for quadratic ( $e^2$ ) weighting in late-types, where  $\sigma/\mu \approx 0.24$  is the coefficient of variation of the ellipticity distribution. The observed values (1.25 for  $\xi_{g+}$  and 1.73 for  $\xi_+$ ) bracket and slightly exceed these predictions, confirming the expected  $e$  and  $e^2$  sensitivity. The modest excess beyond pure statistical expectations for  $\xi_{g+}$  suggests a mixed signal: genuine alignment of disk orientations combined with a contribution from more edge-on systems (which appear more elliptical in projection). For  $\xi_+$ , the strong enrichment reflects the dominance of edge-on disks, which carry both higher ellipticities and stronger shape correlations. Position angles remain clustered near 90–95 across all selections, with no significant systematic offset relative to the full sample, suggesting that the correlation functions are primarily sensitive to the

Table 3: Ellipticity enhancement ratios  $\langle e|SCG \rangle/\langle e \rangle$  for SCGs selected by  $\xi_{g+}(r)$  and  $\xi_+(r)$  at  $R_{25}$ . Expected ratios for linear ( $1 + \sigma/\mu$ ) and quadratic ( $1 + 2\sigma/\mu$ ) scaling are shown for comparison.

Morphology	$\langle e \rangle$	$\xi_{g+}$	$\xi_+$	Linear / Quadratic
Late-type	0.33	1.25	1.73	1.24 / 1.48
Early-type	0.22	1.05	1.95	1.34 / 2.68

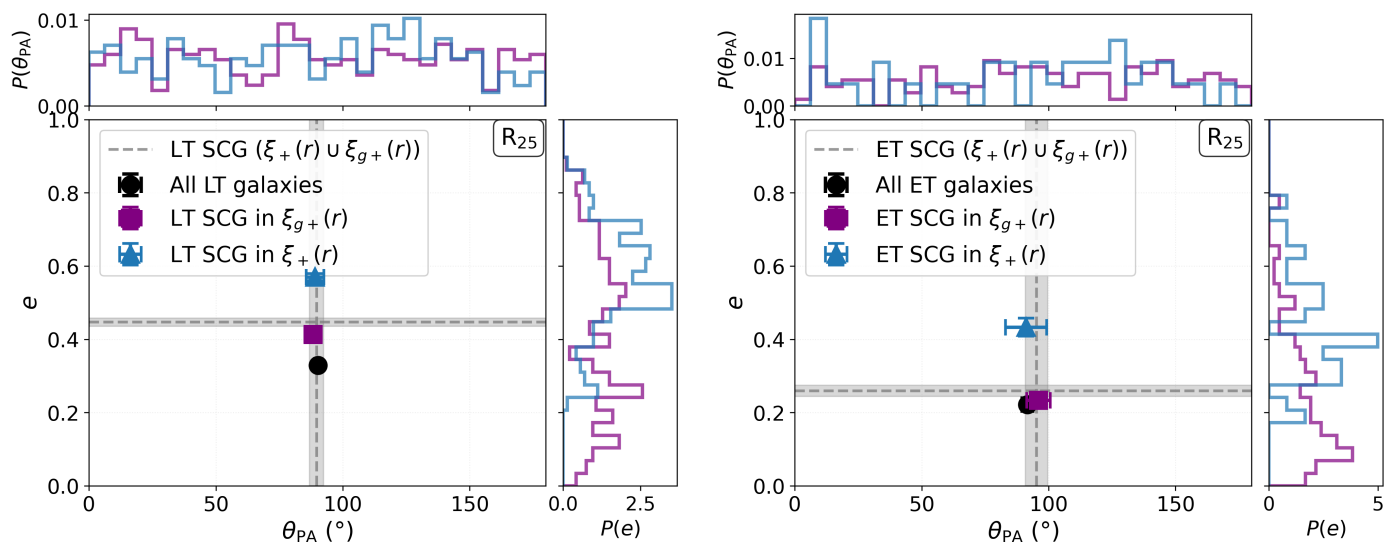


Fig. 6: Morphological properties of SCGs in the ellipticity–position angle plane at  $R_{25}$ : late-type (left) and early-type (right). Black circles show the mean ellipticity and position angle of all galaxies within each morphological class. Colored symbols show the mean positions of SCGs selected by  $\xi_{g+}(r)$  (purple squares) and  $\xi_+(r)$  (blue triangles). Gray dashed lines and shaded regions show the mean and uncertainty of the union of all SCGs ( $\xi_+(r) \cup \xi_{g+}(r)$ ). Top and right panels show marginal distributions  $P(\theta_{PA})$  and  $P(e)$  for each SCG population.

degree of elongation rather than to a preferred orientation on the sky.

For early-types ( $\langle e \rangle \approx 0.22$  for the full subsample), the contrast between the two estimators is striking.  $\xi_{g+}$ -selected SCGs have ellipticities consistent with the full population ( $\langle e \rangle_{SCG} \approx 0.23$ , ratio 1.05), indicating that the density–shape signal is driven by coherent orientations rather than by a selection of intrinsically more elliptical galaxies. This is a “clean” alignment signal, independent of ellipticity. In contrast,  $\xi_+$ -selected SCGs show markedly higher values ( $\langle e \rangle_{SCG} \approx 0.43$ , ratio 1.95), approaching the  $1 + 2\sigma/\mu \approx 2.68$  expectation for quadratic scaling. This reveals that the shape–shape correlation for early-types is dominated by galaxies that have been most strongly deformed by the tidal field. Ellipticity becomes essential for early-types to contribute to  $\xi_+$ , while their contribution to  $\xi_{g+}$  is driven primarily by their biased clustering in dense environments. These conclusions are robust to the choice of isophotal radius.

In summary: for late-types, both estimators show ellipticity enrichment, reflecting the importance of viewing angle (edge-on disks are both more elliptical and better aligned with large-scale structure). For early-types, i)  $\xi_{g+}$  is mostly independent of ellipticity and trace mostly the special location of elliptical galaxies in dense environment and their radial orientation, while ii)  $\xi_+$  shows some ellipticity-dependence hence mixing tidal deformation (which increases ellipticity) with orientation coherence.

### 3.2.4. Environmental distribution of strongly correlated galaxies

Figure 7 shows the environmental positions of SCGs, characterised by their distances to the nearest filament ( $d_{fil}$ ) and nearest cluster or group ( $d_{gr,cl}$ ). Results are consistent across the three isophotal radii.

For late-types, the full sample has mean filament distance  $\sim 5.0$  Mpc and cluster distance  $\sim 6.5$  Mpc. Strongly correlated late-types are systematically closer to filaments (mean

$\sim 3.3$  Mpc, an offset of  $\sim 2$  Mpc) and somewhat closer to clusters ( $\sim 5.5$  Mpc, offset  $\sim 1$  Mpc).

For early-types, the full subsample already lies closer to both structures ( $\sim 2.2$  Mpc from filaments,  $\sim 3.7$  Mpc from clusters)<sup>1</sup>. Strongly correlated early-types are found  $\sim 0.5$  Mpc closer to both filaments and clusters than the full early-type sample.

Figure 7 shows that SCGs are systematically found closer to filaments and clusters than the full sample, but does not reveal whether this environmental preference depends on morphology. Figure 8 addresses this directly by showing the enrichment of early-type and late-type galaxies among SCGs relative to their baseline fractions, as a function of large-scale environment.

For  $\xi_{g+}(r)$ , the morphological mix of SCGs is close to that of the full sample across all environments, confirming the result of Sect. 3.2.2 that morphology alone does not drive selection into the position–shape SCG population. There is however a mild tendency for early-type SCGs to be overrepresented in clusters and groups, where the early-type enrichment rises modestly above unity, while late-type enrichment remains near unity and flat across environments. This is consistent with the picture in which  $\xi_{g+}$  is sensitive to the local density field, which early-types preferentially trace in the densest structures.

For  $\xi_+(r)$ , the picture is strikingly different. Late-type galaxies are strongly overrepresented among SCGs in groups, filaments, and outskirts, with enrichment well above unity, while early-type galaxies fall significantly below unity in all environments except clusters, where both morphologies show comparable enrichment near unity. This depletion of early-type SCGs in underdense environments is especially pronounced: outside clusters, early-type SCGs are rare while late-type SCGs remain abundant. This environmental pattern confirms that shape–shape alignments are driven by a population of coherently elongated late-type galaxies distributed throughout the large-scale structure, rather than by galaxies concentrated in the densest nodes.

<sup>1</sup> This is expected since late-type galaxies are more numerous in smaller filaments not extracted in the coarse DisPerSE reconstruction used here.

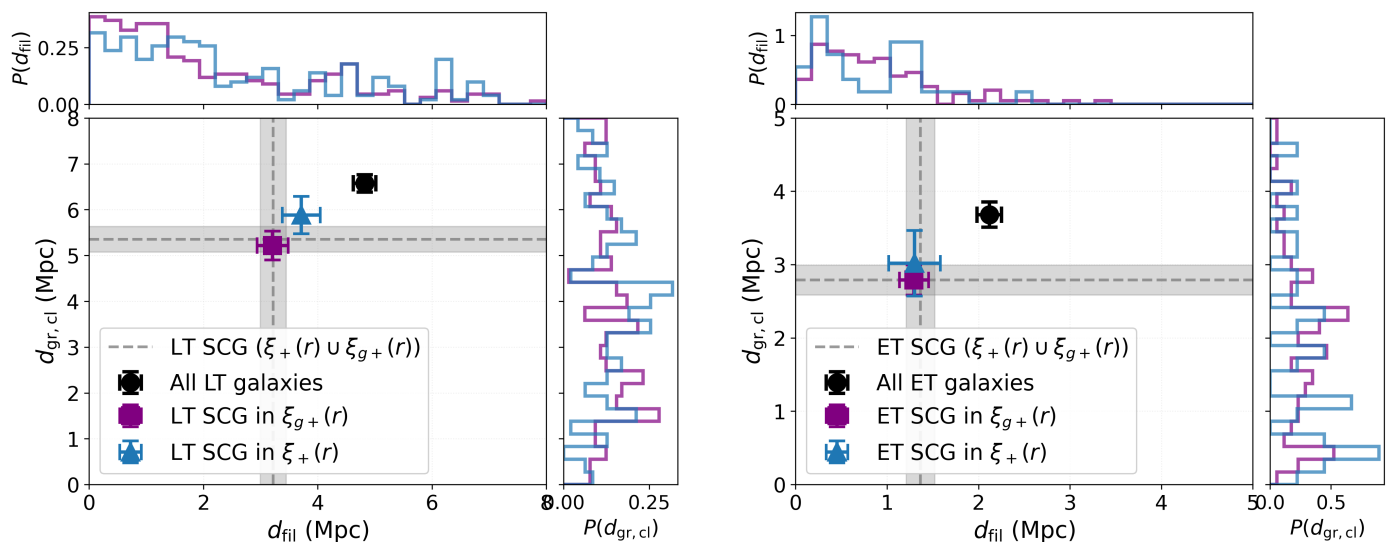


Fig. 7: Mean environmental positions of SCGs with shapes measured at  $R_{25}$ : distance to the nearest filament ( $x$ -axis) vs. distance to the nearest cluster or group ( $y$ -axis) for late-type (left) and early-type (right) galaxies. Black circles show the mean positions of all galaxies within each morphological class. Colored symbols show the mean positions of SCGs selected by  $\xi_{g+}(r)$  (purple squares) and  $\xi_{+}(r)$  (blue triangles). Gray dashed lines and shaded regions show the mean and uncertainty of the union of all SCGs ( $\xi_{+}(r) \cup \xi_{g+}(r)$ ). Top and right panels show marginal distributions  $P(d_{\text{fil}})$  and  $P(d_{\text{gr,cl}})$  for each SCG population.

### 3.3. Direct alignments with the cosmic web

To investigate further the link between intrinsic alignments and the environment, we now study the direct alignments of our sample of galaxies with the cosmic web.

Figure 9 shows the median alignment angle  $\langle \theta \rangle$  between the projected semi-major axis and a reference cosmic-web direction, as a function of morphological type and large-scale environment, for the two mass bins defined in Sect. 2. Error bars are bootstrap uncertainties on the median. Filled circles indicate subsamples with  $n \geq 5$  galaxies; open triangles mark bins with  $n < 5$  and should be interpreted with caution.

Concerning alignment with the cluster direction ( $\theta_{\text{cl}}$ , top row), the clearest signal is seen for elliptical galaxies in clusters, whose median  $\langle \theta_{\text{cl}} \rangle$  lies noticeably below  $45^\circ$  with little dependence on stellar mass. This indicates a tendency for their major axes to point toward the cluster centre, consistent with radial alignment driven by tidal stretching (Joachimi et al. 2015; Hirata et al. 2004). S0 galaxies in clusters show no comparably clear signal, while in groups the situation partially reverses: S0s display a more pronounced offset below  $45^\circ$ , while ellipticals are broadly consistent with isotropy. These morphological differences between clusters and groups are intriguing but remain tentative given the modest sample sizes here in the PPSC. We note that the cluster/group distinction also reflects the different nature of the two surveyed regions: region A, centered on the massive Perseus cluster, contains a higher proportion of evolved clusters, whereas region B exhibits a more diverse mixture of groups and less evolved clusters. This environmental diversity contributes to the observed morphological variations in alignment strength.

Regarding alignment with the filament direction ( $\theta_{\text{fil}}$ , middle and bottom rows), the overall picture is one of isotropy. Most morphological types in most environments are consistent with  $\langle \theta_{\text{fil}} \rangle \approx 45^\circ$  within uncertainties. The only marginal trend appears in filaments of region B, where spiral galaxies show  $\langle \theta_{\text{fil}} \rangle$  slightly above  $45^\circ$ , suggesting a tendency for their major axes to lie perpendicular to the local filament, equivalent to a spin preferentially parallel to the filament spine in the tidal-torque frame-

work (Codis et al. 2012; Welker et al. 2014). No such offset is detected in region A, which contains the massive Perseus cluster whose strong tidal field likely dominates over any coherent filamentary signal. This difference between the two regions should be treated with caution: subsamples are small, projection effects are non-negligible, and a deviation of a few degrees from  $45^\circ$  does not constitute a robust detection in the present dataset.

Taken together, the radial alignment of ellipticals toward cluster centres reinforces the picture emerging from the correlation functions: early-type galaxies in dense environments are preferentially shaped by the local cluster potential. The tentative perpendicular alignment of spirals in region B filaments hints at a spin–filament signal consistent with the low-mass regime of the tidal-torque model (Codis et al. 2012; Joachimi et al. 2015; Castignani et al. 2022), though its statistical significance remains limited by the volume probed and projection effects.

## 4. Discussion

We have measured intrinsic alignment signals in the PPSC using two-point correlation functions at multiple isophotal radii for morphologically stratified samples. The correlation functions extend to  $\sim 0.4\text{--}1 h^{-1}$  Mpc in comoving space, comparable to the characteristic scales of groups and smaller than typical filament radii (Paper I), where tidal fields remain coherent. The use of spectroscopic redshifts is essential for isolating physically associated galaxy pairs and reaching this sensitivity, with direct implications for future surveys combining deep imaging such as Euclid, LSST with spectroscopic campaigns such as DESI (DESI Collaboration et al. 2016; Ivezić et al. 2019).

The alignment signatures show minimal variation across the three isophotal radii  $R_{23}$ ,  $R_{25}$ , and  $R_{27}$ , with only a slight tendency for the large-scale  $\xi_{g+}$  amplitude to increase with increasing  $R_{\text{iso}}$ , consistent with outer isophotes being more sensitive to large-scale tidal distortions (Zjupa & Springel 2017). This near-independence holds despite 10–20% of galaxies showing isophotal twists between consecutive radii, indicating that lo-

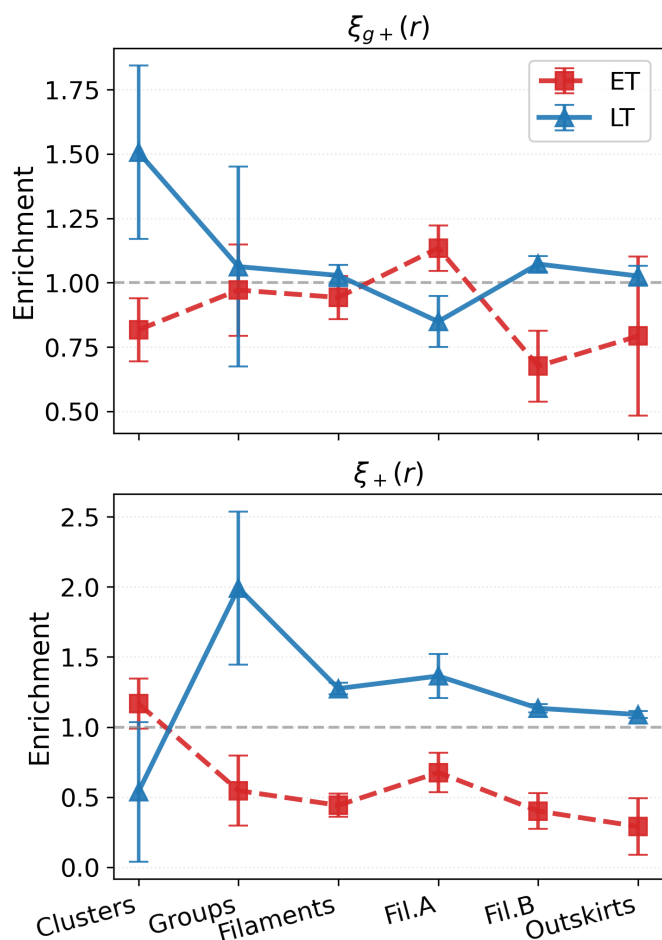


Fig. 8: Morphological enrichment of strongly correlated galaxies (SCGs) as a function of environment at  $R_{25}$ , for  $\xi_{g+}(r)$  (top) and  $\xi_+(r)$  (bottom). The enrichment is defined as the fraction of a given morphological type among SCGs divided by its fraction in the full sample within the same environment. A value above unity indicates over-representation; below unity indicates under-representation. Early-type (ET) galaxies are shown in red; late-type (LT) galaxies in blue.

cal morphological perturbations do not propagate into the statistical alignment signal at population level. Conversely, identifying these isophotal rotations provides a useful diagnostic for systems undergoing local tidal interactions, which could be excluded from correlation measurements in future analyses targeting the purely large-scale tidal signal.

The morphological patterns in the correlation functions and the enrichment analysis (Fig. 8, Sect. 3.2.4) point to two physically distinct alignment mechanisms operating along morphological lines.

For position–shape alignments, the morphological composition of SCGs mirrors that of the full sample at nearly all environments, with only a mild excess of early-types in clusters and groups. This near-neutrality reflects a competition between two opposing effects: the density bias of early-types toward denser environments enhances their contribution to  $\xi_{g+}$ , while their lower ellipticities suppress it, such that the two effects approximately cancel (Chisari et al. 2015). The modest overrepresentation of early-types in the densest environments is consistent with the well-established tendency of pressure-supported

galaxies to align radially toward the halo gravitational potential (Dressler 1980; Joachimi et al. 2015), a one-halo effect driven by tidal interactions with the cluster potential.

For shape–shape alignments, late-type galaxies strongly dominate the SCG population at all environments, with early-types depleted below their baseline fraction, particularly in filaments and outskirts. The systematically higher ellipticities of late-type SCGs ( $e \approx 0.55–0.65$  versus 0.46 for the full late-type sample) are consistent with the  $e^2$  weighting of  $\xi_+$ , which selects the most elongated systems regardless of environment. This behaviour is qualitatively consistent with tidal torque theory, in which large-scale tidal fields coherently spin up disk galaxies during their formation, producing orientations correlated across the filamentary structure (Codis et al. 2012; Welker et al. 2014). A detection of a significant  $\xi_+$  signal for late-type galaxies is noteworthy, as intrinsic alignments in spiral populations have historically been consistent with zero in shallower surveys (Mandelbaum et al. 2006; Joachimi et al. 2015); the deep photometry and extensive spectroscopy of the PPSC dataset are likely key to enabling this detection.

The early-type depletion in  $\xi_+$  outside dense environments deserves particular attention. While early-types are strongly radially aligned toward cluster centres (Sect. 3.3), this intra-halo alignment does not translate into coherent shape–shape correlations between pairs at fixed separation. Their orientations reflect a superposition of radial intra-halo alignments and large-scale tidal alignments pointing in different directions; these can partially cancel in  $\xi_+$  even when the individual  $\xi_{g+}$  signal is strong. This competition is more pronounced in underdense environments where the tidal field is less coherent and the intra-halo signal is absent, leaving early-types with no net preferred orientation relative to their neighbours. This provides a natural and unified explanation for the observed morphological dichotomy.

Our results complement recent direct measurements of galaxy–filament alignments. Muralichandran et al. (2025) studied spin–filament alignments in a much larger sample ( $\sim 32\,500$  spirals and  $\sim 19\,000$  ellipticals from the Siena Galaxy Atlas) and found strong perpendicular alignment for ellipticals ( $\sim 13\sigma$ ) but only weak alignment for spirals ( $\sim 2.8\sigma$ ). The apparent contrast with our detection of a strong late-type  $\xi_+$  signal is not a contradiction: their estimator directly measures the angle between a galaxy’s projected axis and the nearest filament, while  $\xi_+$  measures the mutual coherence of shapes within pairs. A population of disks with spins coherently parallel to filaments will produce both a weak direct spin–filament signal (diluted by projection and line-of-sight contamination) and a strong shape–shape correlation if their ellipticities are high and their orientations are mutually consistent. This complementarity of measurement approaches (Castignani et al. 2022) underscores the value of pair-based statistics in supercluster environments where projection effects are substantial.

Our direct measurements of major-axis alignments with the cosmic web (Sect. 3.3) find results broadly consistent with isotropy, with only a marginal radial alignment of ellipticals toward cluster centres and a tentative perpendicular alignment of spirals in region B filaments. These non-detections are consistent with the volume limitations and projection effects of a single supercluster, and highlight that the pair-based  $\xi_+$  and  $\xi_{g+}$  estimators are more sensitive probes of alignment in this regime.

Strongly correlated galaxies show no systematic mass enhancement relative to the full sample. Mean stellar mass offsets range from +0.04 to +0.05 dex and are consistent with zero within the combined uncertainties, with no coherent trend across morphologies or correlation functions. This suggests that stellar

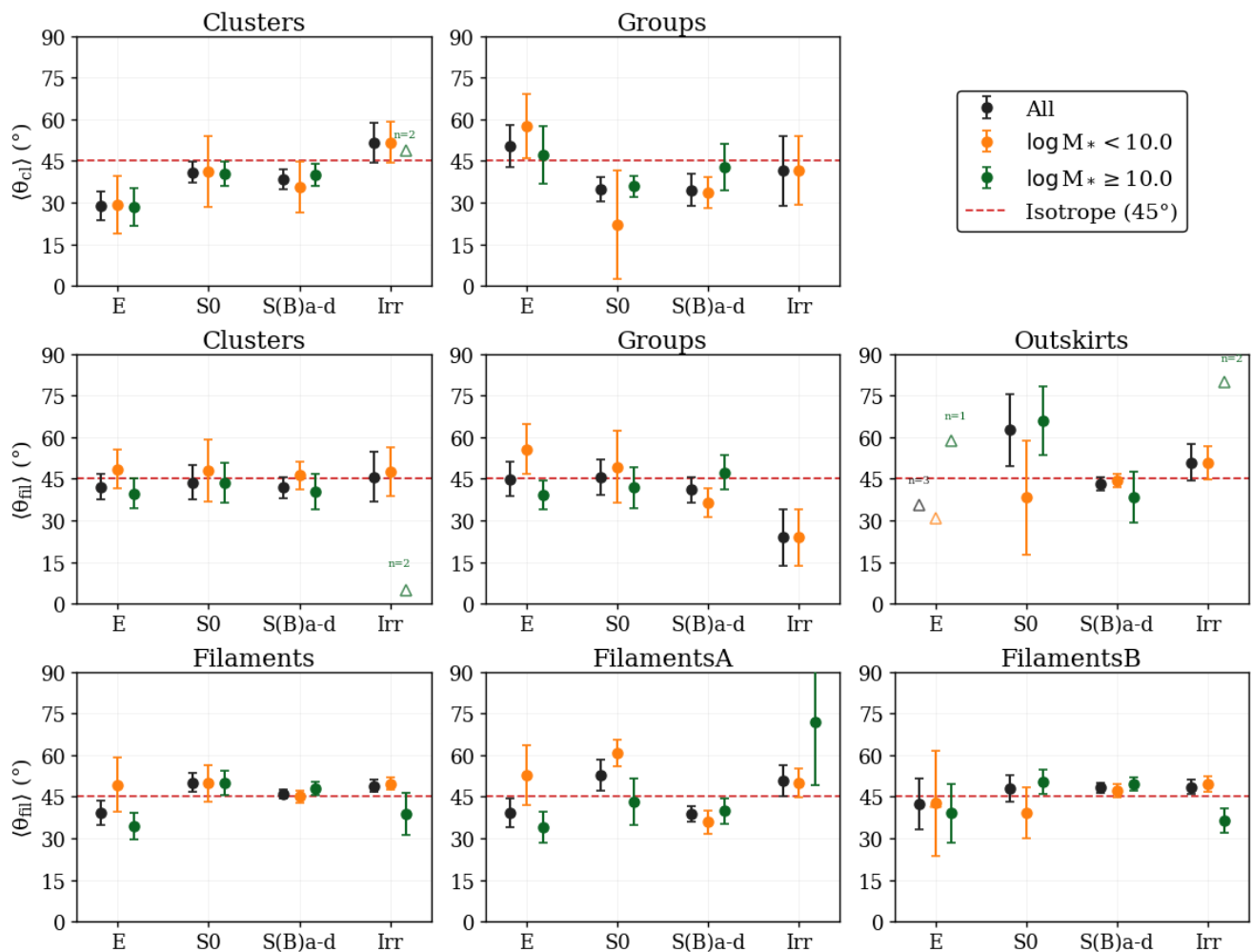


Fig. 9: Median alignment angle between the projected semi-major axis and the cosmic web at  $R_{25}$ , as a function of morphological type (E, S0, S(B)a–d, Irr) and large-scale environment. Top row: angle with the direction to the nearest cluster or group centre ( $\langle\theta_{cl}\rangle$ ) for clusters and groups. Middle row: angle with the nearest filament tangent ( $\langle\theta_{fil}\rangle$ ) for clusters, groups, and outskirts. Bottom row: same for filaments, filaments A (region A), and filaments B (region B). Black points denote the full sample, orange points galaxies with  $\log M_*/M_\odot < 10$ , and dark green points galaxies with  $\log M_*/M_\odot \geq 10$ . The dashed red line at  $45^\circ$  indicates the isotropic expectation.

mass is not a primary driver of alignment strength. However, it is important to distinguish between stellar mass and halo mass in this context. Tidal torque theory predicts that the spin–filament alignment transition occurs at a characteristic halo mass scale (Codis et al. 2012; Welker et al. 2014), not a stellar mass scale; the stellar mass used as a proxy here may therefore dilute any underlying halo-mass dependence, particularly given the scatter in the stellar-to-halo mass relation at these masses. The comparable  $\xi_+$  amplitudes across our two stellar mass bins, combined with findings from Kraljic et al. (2020, 2021) and Barsanti et al. (2022) showing that morphology and bulge fraction correlate more strongly with spin–filament alignments than stellar mass alone, suggest that morphology and environment are the dominant determinants of alignment strength in our sample, with halo mass playing a secondary role that our stellar mass proxy is insufficient to isolate.

## 5. Conclusion

We have presented the first comprehensive study of intrinsic galaxy alignments in the Perseus–Pisces Supercluster, combin-

ing deep low-surface-brightness CFHT  $r$ -band imaging reaching  $28 \text{ mag arcsec}^{-2}$  with the detailed three-dimensional cosmic web reconstruction from Paper I. By measuring galaxy shapes at multiple isophotal radii ( $R_{23}$ ,  $R_{25}$ ,  $R_{27}$ ) and computing their two-point correlation functions in comoving coordinates, we have detected significant intrinsic alignment signals and identified the galaxy populations that contribute most strongly to these correlations.

Our main findings can be summarised as follows:

- Both position-shape  $\xi_{g+}$  and shape-shape  $\xi_+$  correlations show positive signals at separations up to  $\sim 1 \text{ Mpc}/h$  in comoving space, with  $\xi_+$  exhibiting substantially stronger amplitudes ( $S/N \sim 10$  at  $r \lesssim 0.1 h^{-1} \text{ Mpc}$ ) than  $\xi_{g+}$  ( $S/N \sim 3$  at similar scales). Strongly correlated galaxies (SCGs), defined as systems with cumulative pair contributions exceeding one sigma above the mean in the first three comoving separation bins where  $\xi$  is significantly positive, represent only  $\sim 12$ – $19\%$  of the total population.
- Late-type galaxies strongly dominate the shape-shape correlation signal, with  $86\%$  of SCGs in  $\xi_+(r)$  being late-

types despite representing only 69.3% of the sample. Early-types show no significant overrepresentation in position-shape correlations ( $31.0 \pm 2.3\%$  of SCGs in  $\xi_{g+}(r)$  versus their 30.7% baseline fraction), though environmental enrichment becomes clearer when considering their concentration near cluster and group centers. This morphological segregation reflects distinct physical processes: tidal stretching in dense cluster environments for early-types versus coherent tidal torquing along filaments for late-types.

- Strongly correlated late-type galaxies exhibit systematically higher ellipticities ( $e \approx 0.55 - 0.65$ ) than the full sample ( $e \approx 0.46$ ), with minimal systematic offsets in position angle. The observed ellipticity enhancement ratios ( $\langle e_{\text{SCG}} \rangle / \langle e \rangle = 1.25$  for  $\xi_{g+}$  and  $1.73$  for  $\xi_+$ ) are consistent with the expected  $e$  and  $e^2$  weighting of the two estimators, confirming that alignment signals arise from edge-on disk galaxies (whose angular momentum vectors are aligned with the local tidal field) rather than from preferential orientations on the sky.
- Galaxies contributing strongly to correlation functions reside systematically closer to both filament spines (by  $\sim 2$  Mpc for late-types,  $\sim 0.5$  Mpc for early-types) and cluster/group centers (by  $\sim 1$  Mpc for late-types,  $\sim 0.5$  Mpc for early-types) than the full sample. This environmental segregation preserves the morphological stratification documented in Paper I, with aligned early-types concentrated near clusters and groups and aligned late-types preferentially located in filamentary regions where coherent accretion flows are strongest.
- Correlation functions computed at  $R_{23}$ ,  $R_{25}$ , and  $R_{27}$  produce nearly identical profiles, with only a slight tendency for the large-scale  $\xi_{g+}$  amplitude to increase with  $R_{\text{iso}}$ , consistent with outer isophotes being more sensitive to large-scale tidal distortions. This near-independence holds despite 10–20% of galaxies showing ellipticity changes and position angle rotations between consecutive radii.

These results complement recent observational measurements in spiral populations (Welker et al. 2020; Kraljic et al. 2021; Muralichandran et al. 2025) and demonstrate the value of combining photometric shapes with spectroscopic redshifts for upcoming surveys like *Euclid* (Laureijs et al. 2011; Euclid Collaboration et al. 2025c), DESI (DESI Collaboration et al. 2016), and LSST (Ivezic et al. 2019). The observed morphology-dependent patterns reinforce the need for weak lensing analyses to account for galaxy type and environment when modeling intrinsic alignment systematics, including blue/late-type galaxies.

Key limitations include modest sample size, restriction to a single supercluster environment, and large uncertainties for early-type subsamples in underdense regions. Our inability to detect direct galaxy-filament alignment angles, unlike Muralichandran et al. (2025), highlights the complementary nature of statistical pair correlations versus direct geometric measurements (Castignani et al. 2022). Future work extending these measurements to diverse local superclusters with *Euclid* first data release will assess how representative our findings are, though well-characterized local benchmarks remain essential for calibrating large statistical samples. The combination of *Euclid*'s exquisite image quality and optimized low-surface-brightness processing (Cuillandre et al. 2024, 2025) will enable shape measurements extending to  $R_{29}$  and beyond, probing alignment signals in the outermost stellar halos where tidal coupling to the cosmic web is expected to be strongest. Early results from the Perseus-Pisces region observed during *Euclid* Early Release Ob-

servations (Mondelin et al. 2025) demonstrate the potential for such deep measurements across multiple nearby superclusters.

## References

- Aragón-Calvo, M. A., van de Weygaert, R., Jones, B. J. T., & van der Hulst, J. M. 2007, *ApJ*, 655, L5
- Barsanti, S., Colless, M., Welker, C., et al. 2022, *Monthly Notices of the Royal Astronomical Society*, 516, 3569
- Bartelmann, M. & Schneider, P. 2001, *Phys. Rep.*, 340, 291
- Blazek, J., McQuinn, M., & Seljak, U. 2011, *J. Cosmology Astropart. Phys.*, 2011, 010
- Blazek, J. A., MacCrann, N., Troxel, M. A., & Fang, X. 2019, *Phys. Rev. D*, 100, 103506
- Bond, J. R., Kofman, L., & Pogosyan, D. 1996, *Nature*, 380, 603
- Castignani, G., Vulcani, B., Finn, R. A., et al. 2022, *ApJS*, 259, 43
- Catelan, P. & Porciani, C. 2001, *MNRAS*, 323, 713
- Chisari, N., Codis, S., Laigle, C., et al. 2015, *MNRAS*, 454, 2736
- Chisari, N. E. 2025, *The Astronomy and Astrophysics Review*, 33
- Chisari, N. E., Koukoufilippas, N., Jindal, A., et al. 2017, *MNRAS*, 472, 1163
- Codis, S., Gavazzi, R., Dubois, Y., et al. 2015a, *MNRAS*, 448, 3391
- Codis, S., Jindal, A., Chisari, N. E., et al. 2018, *MNRAS*, 481, 4753
- Codis, S., Pichon, C., Devriendt, J., et al. 2012, *MNRAS*, 427, 3320
- Codis, S., Pichon, C., & Pogosyan, D. 2015b, *MNRAS*, 452, 3369
- Cuillandre, J.-C., Bertin, E., Bolzonella, M., et al. 2025, *A&A*, 697, A6
- Cuillandre, J.-C., Bolzonella, M., Boselli, A., et al. 2024, *A&A*, this issue
- Dark Energy Survey and Kilo-Degree Survey Collaboration, Abbott, T. M. C., Aguena, M., et al. 2023, *The Open Journal of Astrophysics*, 6, 36
- DESI Collaboration, Aghamousa, A., Aguilar, J., et al. 2016, *arXiv e-prints*, arXiv:1611.00036
- Doroshkevich, A. G. 1970, *Astrophysics*, 6, 320
- Dressler, A. 1980, *ApJ*, 236, 351
- Dubois, Y., Pichon, C., Welker, C., et al. 2014, *MNRAS*, 444, 1453
- Euclid Collaboration, Aussel, H., Tereno, I., et al. 2025a, *arXiv e-prints*, arXiv:2503.15302
- Euclid Collaboration, Laigle, C., Gouin, C., et al. 2025b, *arXiv e-prints*, arXiv:2503.15333
- Euclid Collaboration, Mellier, Y., Abdurro'uf, et al. 2025c, *A&A*, 697, A1
- Euclid Collaboration: Mellier, Y., Abdurro'uf, Acevedo Barroso, J., Achúcarro, A., et al. 2025, *A&A*, this issue
- Ferrarese, L., Côté, P., Cuillandre, J.-C., et al. 2012, *ApJS*, 200, 4
- Gwyn, S., McConnachie, A. W., Cuillandre, J.-C., et al. 2025, *AJ*, 170, 324
- Hahn, O., Teyssier, R., & Carollo, C. M. 2010, *MNRAS*, 405, 274
- Hervas Peters, F., Kilbinger, M., Paviot, R., et al. 2025, *A&A*, 699, A201
- Hildebrandt, H., Erben, T., Kuijken, K., et al. 2012, *MNRAS*, 421, 2355
- Hirata, C. M., Mandelbaum, R., Seljak, U., et al. 2004, *MNRAS*, 353, 529
- Ivezic, Z., Kahn, S. M., Tyson, J. A., et al. 2019, *The Astrophysical Journal*, 873, 111
- Jarvis, M. 2015, *TreeCorr: Two-point correlation functions*, *Astrophysics Source Code Library*, record ascl:1508.007
- Joachimi, B., Cacciato, M., Kitching, T. D., et al. 2015, *Space Sci. Rev.*, 193, 1
- Joachimi, B., Mandelbaum, R., Abdalla, F. B., & Bridle, S. L. 2011, *A&A*, 527, A26
- Kiessling, A., Cacciato, M., Joachimi, B., et al. 2015, *Space Sci. Rev.*, 193, 67
- Kilbinger, M. 2015, *Reports on Progress in Physics*, 78, 086901
- Klypin, A. A. & Shandarin, S. F. 1983, *MNRAS*, 204, 891
- Kraljic, K., Davé, R., & Pichon, C. 2020, *MNRAS*, 493, 362
- Kraljic, K., Duckworth, C., Tojeiro, R., et al. 2021, *MNRAS*, 504, 4626
- Laigle, C., Pichon, C., Codis, S., et al. 2015, *MNRAS*, 446, 2744
- Lamman, C., Tsaprazi, E., Shi, J., et al. 2024, *The Open Journal of Astrophysics*, 7, 14
- Laureijs, R., Amiaux, J., Arduini, S., et al. 2011, *arXiv e-prints*, arXiv:1110.3193
- Mandelbaum, R. 2018, *ARA&A*, 56, 393
- Mandelbaum, R., Hirata, C. M., Ishak, M., & Seljak, U. 2006, in *American Astronomical Society Meeting Abstracts*, Vol. 209, *American Astronomical Society Meeting Abstracts*, 77.27
- Mondelin, M., Bournaud, F., Cuillandre, J. C., et al. 2025, *A&A*, 699, A214
- More, S., Sugiyama, S., Miyatake, H., et al. 2023, *Phys. Rev. D*, 108, 123520
- Muralichandran, Y., Libeskind, N. I., & Tempel, E. 2025, *A&A*, 703, A11
- Navarro-Gironés, D., Crocce, M., Gaztañaga, E., et al. 2026, *MNRAS*, 545, staf1630
- Peebles, P. J. E. 1969, *ApJ*, 155, 393
- Peng, Y.-K., Lilly, S. J., Kovač, K., & et al. 2010, *The Astrophysical Journal*, 721, 193
- Regaldo-Saint Blancard, B., Codis, S., Bond, J. R., & Stein, G. 2021, *MNRAS*, 504, 1694
- Singh, S., Mandelbaum, R., & More, S. 2015, *MNRAS*, 450, 2195

- Singh, S., Shakir, A., Jagvaral, Y., & Mandelbaum, R. 2024, Increasing the power of weak lensing survey data with multipole-based intrinsic alignment estimators
- Sousbie, T., Pichon, C., & Kawahara, H. 2011, MNRAS, 414, 384
- Stone, C. J., Arora, N., Courteau, S., & Cuillandre, J.-C. 2021, MNRAS, 508, 1870
- Stone, C. J., Courteau, S., Cuillandre, J.-C., et al. 2023, MNRAS, 525, 6377
- Troxel, M. A. & Ishak, M. 2015, Phys. Rep., 558, 1
- Tudorache, M. N., Jung, S. L., Jarvis, M. J., et al. 2025, MNRAS, 544, 4306
- Welker, C., Bland-Hawthorn, J., van de Sande, J., et al. 2020, MNRAS, 491, 2864
- Welker, C., Devriendt, J., Dubois, Y., Pichon, C., & Peirani, S. 2014, MNRAS, 445, L46
- Welker, C., Dubois, Y., Pichon, C., Devriendt, J., & Chisari, N. E. 2018, A&A, 613, A4
- York, D. G., Adelman, J., Anderson, Jr., J. E., et al. 2000, AJ, 120, 1579
- Zjupa, J., Paranjape, A., Hahn, O., & Pakmor, R. 2020, arXiv e-prints, arXiv:2009.03329
- Zjupa, J. & Springel, V. 2017, MNRAS, 466, 1625

*Acknowledgements.* Based on observations obtained at the Canada-France-Hawai'i Telescope (CFHT) which is operated by the National Research Council of Canada, the Institut National des Sciences de l'Univers of the Centre National de la Recherche Scientifique of France, and the University of Hawai'i. CFHT is located on Maunakea on Hawai'i Island, a mountain of considerable cultural, natural, and ecological significance. Maunakea is a sacred site to Native Hawaiians, also known as Kānaka 'Ōiwi. Quality observations are made possible by relentless effort of the entire staff at Canada-France-Hawai'i Telescope. Based on observations obtained with MegaPrime/MegaCam, a joint project of CFHT and CEA/DAPNIA.

This research is based in part on data collected at Subaru Telescope, which is operated by the National Astronomical Observatory of Japan. Pan-STARRS is a project of the Institute for Astronomy of the University of Hawaii, and is supported by the NASA SSO Near Earth Observation Program under grants 80NSSC18K0971, NNX14AM74G, NNX12AR65G, NNX13AQ47G, NNX08AR22G, 80NSSC21K1572, and by the State of Hawaii. This research used the facilities of the Canadian Astronomy Data Centre operated by the National Research Council of Canada with the support of the Canadian Space Agency. Additionally, we are grateful for the computing resources of the Digital Research Alliance of Canada and the CANFAR (Canadian Advanced Network for Astronomical Research) Science Portal for enabling the analysis in this paper.

This research has made use of the NASA/IPAC Extragalactic Database (NED), which is operated by the Jet Propulsion Laboratory, California Institute of Technology, under contract with the National Aeronautics and Space Administration. We also acknowledge the use of the HyperLEDA database, the tools and catalogs provided by the CDS, and the publicly available data from the 2MRS, SDSS, and FASHI surveys, which were essential for the analyses presented in this work.

We thank Florence Durret for her insightful comments and suggestions that improved this paper.

This work was also supported by the CEA Research Funding (Contrat formation par la recherche) program.

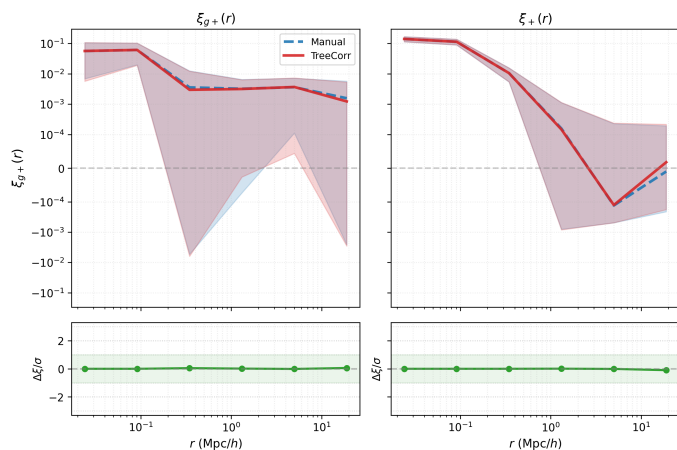


Fig. A.1: Validation of manual shear correlation functions (blue dashed) against TreeCorr (red solid) at  $R_{25}$ . Top:  $\xi_{g+}$  (left) and  $\xi_+$  (right) in comoving coordinates. Shaded regions show errors. Bottom: Normalized differences ( $\Delta\xi/\sigma$ ). All measurements agree within  $\pm 1\sigma$  (green band), confirming our manual implementation.

## Appendix A: Comparison TreeCorr and manual computation

Figure A.1 validates our manual correlation implementations against TreeCorr (Jarvis 2015) at  $R_{25}$ . Both methods employ identical jackknife resampling for error estimation. The lower panels display normalized differences ( $\Delta\xi/\sigma_{\text{combined}}$ ), showing that all measurements agree within  $\pm 1\sigma$  (green band).

## Appendix B: Morphology of galaxies

Figure B.1 shows the projected distribution of galaxies in the PPSC colour-coded by morphological type. This figure provides a visual complement to the quantitative environmental trends discussed in Sect. 3.2.4. Early-type galaxies are preferentially located in the densest regions, in particular around cluster and group centres, whereas late-type galaxies are more broadly distributed along filamentary structures and in the outskirts. This projected morphology–environment segregation is consistent with the environmental classification inherited from Paper I and supports the interpretation that the alignment signal depends not only on morphology, but also on where each morphological population resides within the cosmic web.

The figure also highlights the different spatial sampling of the two observed regions. Region A contains a more prominent concentration of early-type galaxies associated with the dense cluster environment. Region B shows a more extended distribution of late-type galaxies along lower-density filamentary structures. These differences motivate the separate discussion of direct filament alignments in regions A and B in Sect. 3.3.

## Appendix C: Morphology-dependent correlation functions

Figure C.1 presents correlation functions computed separately for different morphological cross-correlations measured at  $R_{25}$ . The upper row shows  $\xi_{g+}(r)$  for ET×all (left) and LT×all (right), measuring position-shape correlations between galaxies of a specific morphological type (late or early type) as shape tracers

and the full galaxy population as density tracers. The lower row shows  $\xi_+(r)$  for ET×ET (left) and LT×LT (right), measuring shape-shape correlations within each morphological type.

These decomposed correlation functions reveal that late-type galaxies clearly dominate the intrinsic alignment signal, while early-type correlations suffer from large uncertainties that prevent robust conclusions. For ET×all, the  $\xi_{g+}(r)$  measurement shows large uncertainties across all scales, making it difficult to assess the contribution of early-types to the position-shape signal. Similarly, the ET×ET shape-shape correlation  $\xi_+(r)$  exhibits uncertainties comparable to or exceeding the signal amplitude, precluding a meaningful detection.

By contrast, LT×all shows a clear positive  $\xi_{g+}(r)$  signal extending at least to  $r \sim 0.1 h^{-1}$  Mpc, with amplitudes reaching  $\sim 9 \times 10^{-2}$  at small separations before declining toward the baseline. This confirms that late-type galaxies contribute significantly to the position-shape correlation measured for the full sample (Fig. 5).

The LT×LT shape-shape correlation  $\xi_+(r)$  provides the most striking result: a robust positive signal with amplitudes of  $\sim 0.1$ – $0.2$  at  $r \lesssim 0.1 h^{-1}$  Mpc, remaining significantly positive out to  $\sim 0.4 h^{-1}$  Mpc. This demonstrates that the strong  $\xi_+$  signal detected in the full sample (Fig. 5) is carried almost entirely by the late-type population. The extended correlation scale ( $\sim 0.4 h^{-1}$  Mpc) indicates that late-type shape alignments persist well beyond the one-halo regime, consistent with coherent tidal torquing along filamentary structures where late-types preferentially reside (Sect. 3.2.4).

These findings confirm the morphological dichotomy identified in Sect. 3.2: shape-shape alignment signals are dominated by late-type galaxies, whose high ellipticities (reflecting preferentially edge-on configurations) and coherent orientations along the cosmic web produce strong mutual shape correlations. The inability to robustly detect ET×ET correlations does not imply that early-type galaxies are unaligned, but rather reflects the smaller sample size, lower mean ellipticities, and the potential cancellation between radial alignments toward cluster centers and large-scale tidal alignments discussed in Sect. 4.

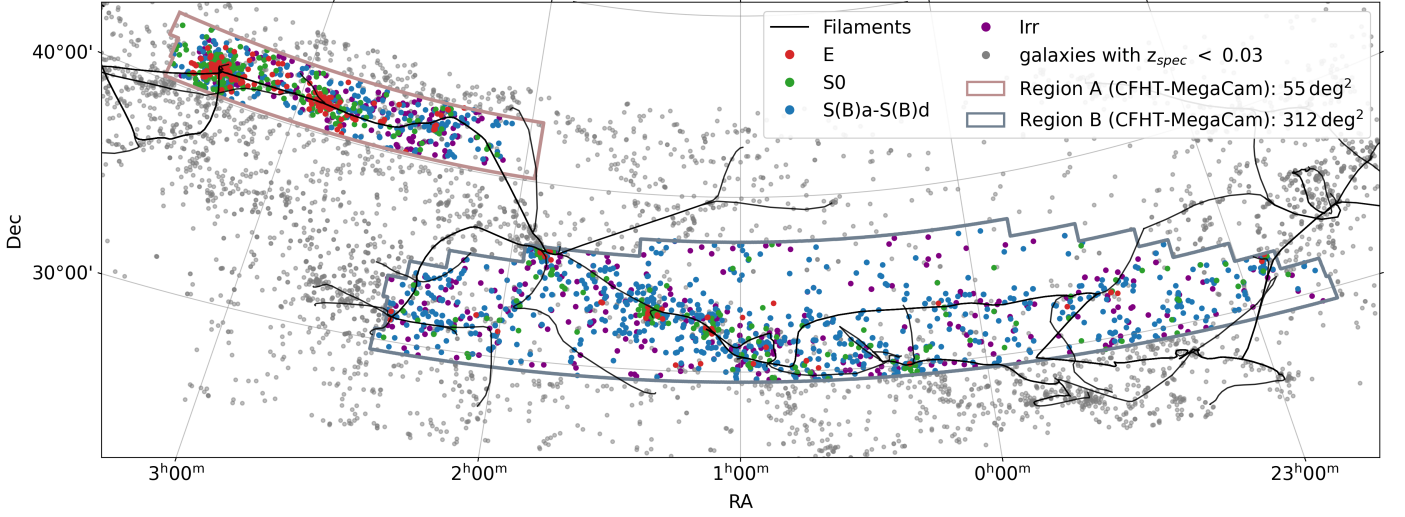


Fig. B.1: Projected distribution of galaxies in the PPSC colour-coded by morphological type. Grey points show the full galaxy catalogue, coloured points indicate galaxies with morphological classifications, and black curves trace the projected 3D cosmic-web skeleton from Paper I.

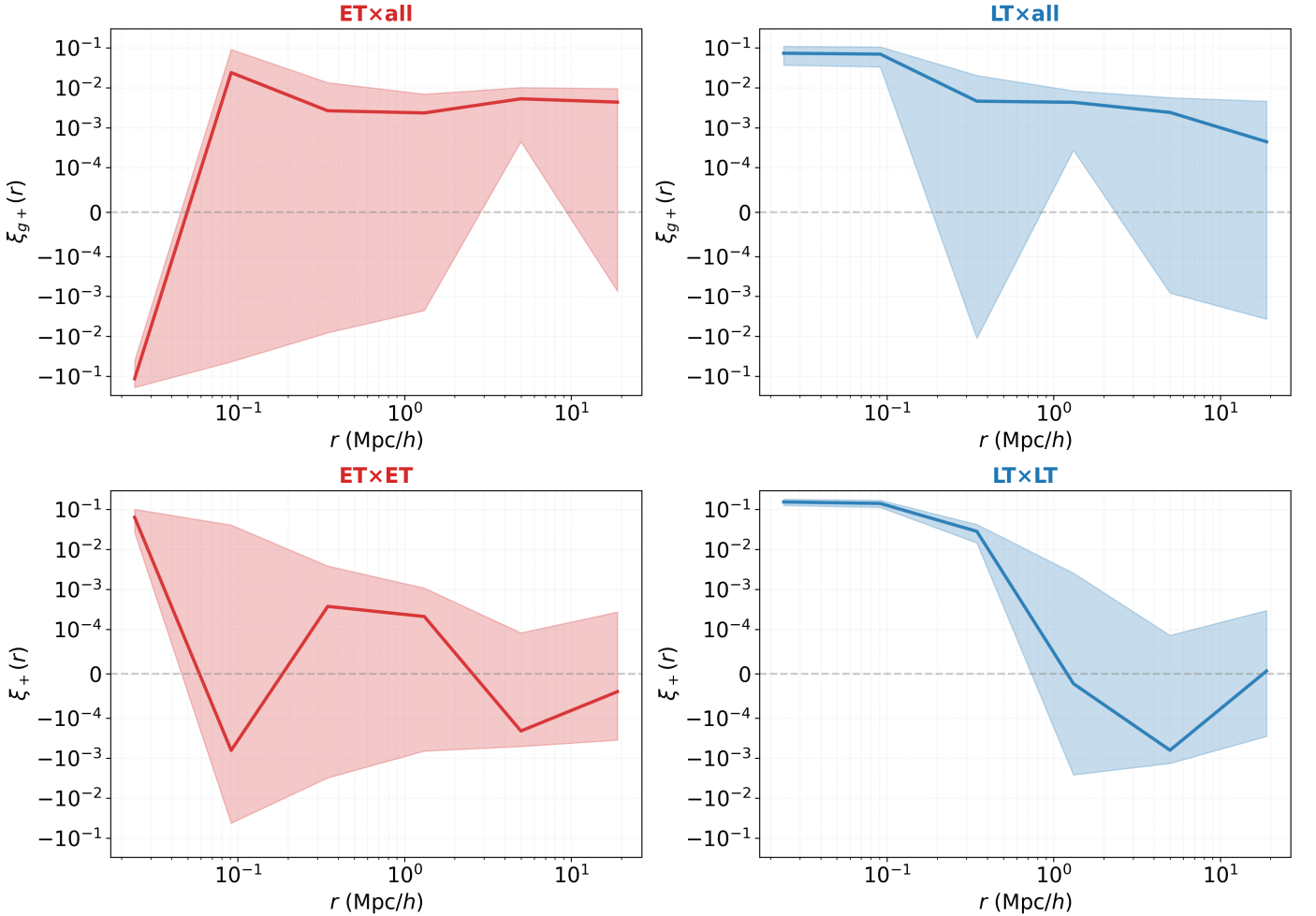


Fig. C.1: Morphology-dependent correlation functions at  $R_{25}$ . Upper row: position-shape correlation  $\xi_{g+}(r)$  for ET×all (left, red) and LT×all (right, blue). Lower row: shape-shape correlation  $\xi_{+}(r)$  for ET×ET (left, red) and LT×LT (right, blue). Shaded regions indicate bootstrap uncertainties. The dashed grey line marks zero correlation.